Check for updates

Small

NANO · MICRO small
www.small-journal.com

RESEARCH ARTICLE

Hydrogen-Bond Reinforced Composite Electrolytes for Room-/Subzero-Temperature, Highly Stable Lithium Metal Batteries

Dongmei Zhang | Jiangping Zhang | Baoyi Wang | Jiaxin Tu | Rubing Xu | Mengxuan Zhang | Lehao Liu | Qianxiao Fan | Meicheng Li

State Key Laboratory of Alternate Electrical Power System With Renewable Energy Sources, School of New Energy, North China Electric Power University, Beijing, China

Correspondence: Lehao Liu (lehaoliu@ncepu.edu.cn) | Meicheng Li (mcli@ncepu.edu.cn)

Received: 14 January 2026 | **Revised:** 8 March 2026 | **Accepted:** 26 March 2026

Keywords: all-solid-state lithium metal battery | compatibility | composite electrolyte | silica nanosphere

ABSTRACT

Succinonitrile (SN)-based electrolytes with high ionic conductivity are considered as a promising candidate for all-solid-state lithium metal batteries (LMBs). However, the decomposition of SN on the lithium metal electrode surfaces severely challenges the stable operation of LMBs. Herein, this work introduces a hydrogen-bond strategy to enhance the cycling stability of SN electrolyte-based LMBs by incorporating accessible aramid nanofibers (ANFs) and amino-functionalized silica (SiO_2—NH_2) nanospheres into the electrolyte. The -NH groups of the ANFs and the -NH_2 groups of the SiO_2—NH_2 establish multiple hydrogen-bonds with the -C≡N groups of SN in the electrolyte, suppressing SN decomposition and blocking the deleterious SN-lithium metal interaction. Additionally, the composite electrolyte facilitates uniform Li^+ deposition on the lithium electrodes and inhibits dendrite growth. Consequently, the composite electrolyte-based Li||Li symmetrical cells display an exceptional cyclic durability, surpassing 2600 h. Furthermore, the electrolyte-based Li||$LiFePO_4$ cells present excellent cycling stability for 700 cycles at room temperature and 0°C. The solid-state Li||$LiNi_{0.6}Co_{0.2}Mn_{0.2}O_2$ cells with a high active mass loading of 10 mg cm^{-2} also deliver superior cycle performance. This work adopts the multiple hydrogen-bond interaction for highly stable SN-based solid-state LMBs.

1 | Introduction

Lithium-ion batteries (LIBs) have been used in numerous fields, including digital devices, electric vehicles, and residential back-up power [1, 2]. Nevertheless, traditional LIBs cannot meet the growing energy demand because of the limited energy density of the electrode materials based on the insertion mechanism. Lithium metal has garnered intense interest as an anode candidate owing to the merits of the ultrahigh specific capacity (3860 mAh g^{-1}) and ultralow redox potential (−3.04 V vs Li^+/Li) [3]. On the other hand, the application of lithium metal batteries (LMBs) with commercial carbonate or ether electrolytes has been hindered by safety concerns such as the high flammability of the liquid electrolytes, dendrite growth, and unstable solid electrolyte interphase (SEI) [4].

All-solid-state LMBs hold great promise in solving the above-mentioned issues by replacing the flammable liquid electrolytes with high-modulus solid-state electrolytes (SSEs). Among various candidates, the inorganic ceramic electrolytes suffer from poor electrode/electrolyte interface contact, severely hindering their practical application [5–7]. Meanwhile, the insufficient ionic conductivity of the solid polymer electrolytes greatly limited the delivery of power in LMBs [8, 9]. Therefore, it is significant to

© 2026 Wiley-VCH GmbH

explore electrolytes with superior interface contact and high ionic conductivity to boost the performance of the LMBs.

The plastic crystal electrolyte based on succinonitrile (SN) is considered a potential electrolyte system due to its outstanding ionic conductivity, softness, and inherently non-flammable nature [10, 11]. However, it is noteworthy that the poor reductive stability of SN molecules constantly causes serious interface corrosion of lithium metal. In addition, under the catalysis of the lithium metal, the strong electron-withdrawing -C≡N groups can significantly boost the activity of α-H to produce hydrogen gas along with other by-products, triggering the successive decomposition of the electrolytes and rapid decay of the battery performance [9, 12]. To solve the above-mentioned challenges, research efforts have increasingly focused on the design of a dual-salt electrolyte system. The utilization of dual-salt electrolytes inhibits the side reactions between SN and lithium metal by promoting the formation of a robust and conducive SEI layer at the lithium metal surface. [9, 13–17] However, the high cost of lithium salts brings about an adverse effect for the commercialization of the SN-based electrolytes. On the other hand, many studies have explored the hydrogen-bond interaction between the α-H atoms of SN and oxygen-rich groups of the introducing electrolyte components in SN-based electrolytes, which effectively weakens the decomposition of SN and the corrosion of lithium metal [11, 12, 18, 19]. However, current research on SN-based electrolytes has focused exclusively on the coordination interaction of α-H atoms, neglecting the strong electron-withdrawing -C≡N groups of SN. Additionally, these electrolyte components typically suffer from complex fabrication processes, limiting their practical application in LMBs. Therefore, using accessible and cost-effective electrolyte components with electron-donating groups to directly interact with -C≡N groups would be another effective route to boost the electrochemical compatibility of the SN with lithium metal.

Benefiting from the abundant silica sources and the mature technology for large-scale fabrication of nanoparticles, the mesoporous amino-functionalized silica (SiO_2—NH_2) nanospheres with strong electron-donating -NH_2 groups have been widely investigated as fillers in solid polymer electrolytes to accelerate lithium salts dissociation and suppress lithium dendrite growth [20]. In addition, aramid nanofibers (ANFs) with abundant polar amide groups, large aspect ratio, high mechanical strength, and low electro-conductivity have been used as multifunctional nanofillers to improve the electrical and mechanical properties of the solid polymer electrolytes [21, 22]. Herein, we design a novel SN-based composite electrolyte containing ANFs and SiO_2—NH_2 nanospheres to directly interact with the -C≡N groups of SN (Figure 1a). The strong hydrogen-bond between the -C≡N groups of SN and the -NH groups of the ANFs and the -NH_2 groups of the SiO_2—NH_2 can inhibit the decomposition of SN, greatly enhancing the electrochemical compatibility of SN with lithium metal. As a result, the composite electrolyte exhibits a superior Li^+ transference number of 0.79 and Li^+ conductivity of 7.55×10^{-4} S cm^{-1} at 30°C. Significantly, the composite electrolyte-based Li||Li symmetrical cells operate for a long lifespan of 2600 h. The solid-state Li||$LiFePO_4$ cells and Li||$LiNi_{0.6}Co_{0.2}Mn_{0.2}O_2$ cells also deliver excellent cycling stability and rate performance at room temperature and even at a low temperature of 0°C.

2 | Results and Discussion

2.1 | Microstructure of Composite Electrolytes

The composite electrolytes were prepared by a conventional vacuum filtration method (Figure 1b). First, the ANF solution and the SiO_2—NH_2 nanosphere solution were mixed, and then the porous ANF-based substrate films (i.e., ANF0, ANF5, and ANF10) were prepared with various contents of SiO_2—NH_2 nanofillers (0, 5, and 10 wt.%) by filtering the ANF and SiO_2—NH_2 mixture solution. The SiO_2—NH_2 nanofillers showed a type IV adsorption–desorption isotherm with a mixed hysteresis loop of H2 and H3, demonstrating the existence of micropores, mesopores, and macropores (Figure S1). Simultaneously, the mesoporous SiO_2—NH_2 nanospheres exhibited a high specific surface area of 174.9 m^2 g^{-1}, which was conducive to providing more active sites (Figure S2). And the surface of the ANF5 films exhibited a porous structure (Figures S3 and S4). However, with the increasing content of the nanofillers to 10 wt.%, the porous structure of the films disappeared. The surface and cross-sectional scanning electron microscopy (SEM) images of the ANF10 films showed the agglomeration of the SiO_2—NH_2 nanofillers.

The SN-lithium bis (trifluoromethyl sulphonyl) imide (LiTFSI) electrolyte was prepared with a molar ratio of 20:1 to guarantee high ionic conductivity [10]. The molten SN-LiTFSI electrolyte was filled into the porous ANF-based substrate films by the second vacuum filtration. The composite electrolytes were obtained with various ANF-based substrate films (i.e., CPE0, CPE5, and CPE10). The CPE5 membranes had a high content of the SN-LiTFSI electrolyte (~55 wt.%) (Table S1). As shown in Figure 1c, compared with the ANF5 films, the CPE5 membranes were completely filled with SN-LiTFSI electrolyte without any obvious pores. Meanwhile, the corresponding energy dispersive spectral (EDS) mapping of the CPE5 membranes further verified that the porous ANF5 substrate films were fully filled with the SN-LiTFSI electrolyte, and the SiO_2—NH_2 nanoparticles were evenly dispersed in the CPE5 membranes. Finally, the obtained CPE5 membranes possessed a small thickness of 34 μm (twice that of the ANF5 films), which was comparable to that of commercial separators. In addition, the CPE5 membranes showed high flexibility, and they can be folded and unfolded many times without fracture (Figure S5).

2.2 | Anchoring SN by Hydrogen-Bond Interaction

Theoretical calculations and characterization techniques were employed to investigate the crucial role of hydrogen-bond interaction in anchoring SN and inhibiting the decomposition of SN. As shown in Figure 2a, the electrostatic potential (ESP) was obtained to analyze the electron distribution of the SN molecules, which can reveal the molecular coordination between SN and other components of the composite electrolytes. The electron density of the electron-withdrawing -C≡N groups in SN was reduced significantly, demonstrating that the polar groups of the ANF and the SiO_2—NH_2 can coordinate with the -C≡N groups of SN, weakening the dipole–dipole interaction of SN and reducing the activity of the α-H atom in SN. To further analyze the coordination in different electrolyte systems, the

16136829, 2026, 29, Downloaded from https://onlinelibrary.wiley.com/doi/10.1002/smll.73296 by North China Electric Power University Beijing, Wiley Online Library on [08/10/2026]. See the Terms and Conditions (https://onlinelibrary.wiley.com/terms-and-conditions) on Wiley Online Library for rules of use; OA articles are governed by the applicable Creative Commons License

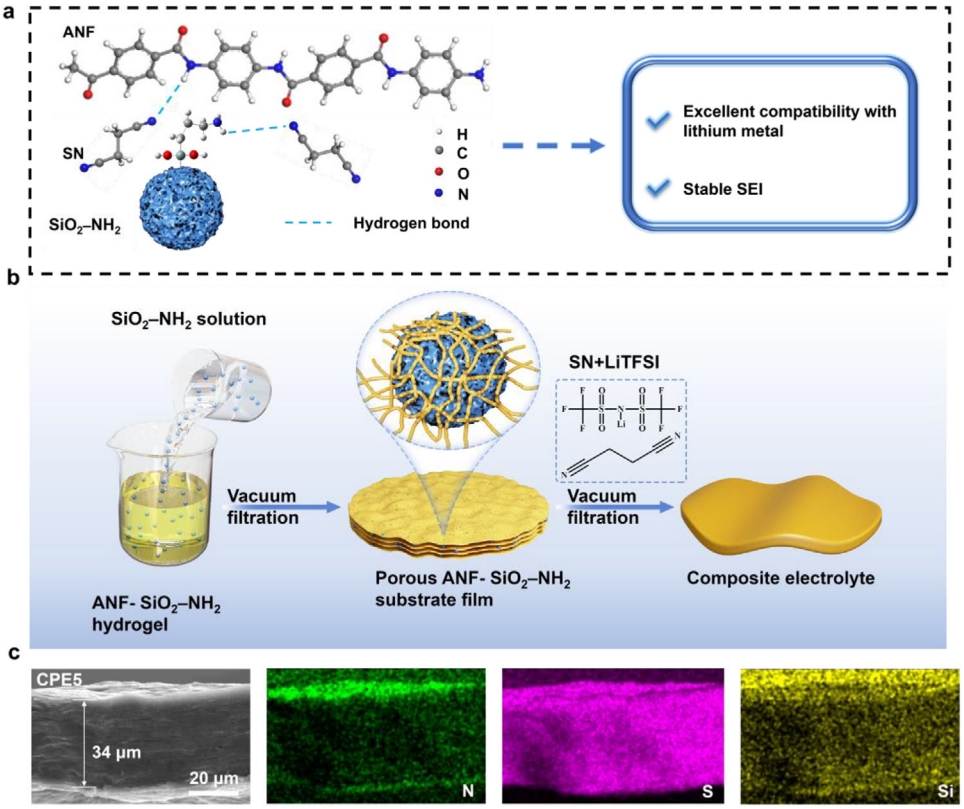


FIGURE 1 | Schematic diagram of the preparation process and characterization of the composite electrolyte membranes. (a) Schematic illustration of the interaction between the SiO_2—NH_2, ANF, and SN for enhancing the compatibility of SN with lithium metal. (b) Schematic illustration of the preparation of a composite electrolyte by the vacuum filtration method. (c) Cross-sectional SEM image of the CPE5 membranes with corresponding EDS element mappings of the N, S, and Si elements.

binding energy of optimized geometric configurations was also calculated based on density functional theory (DFT) (Figure 2b). The binding energy between SN and ANF was —0.32 eV, while the binding energy between SN and SN was —0.23 eV, indicating that SN can easily interact with ANF and be absorbed on the ANF chains. Moreover, the binding energy between SiO_2—NH_2 and SN was the lowest (—0.39 eV), demonstrating that SN tended to coordinate with SiO_2—NH_2. Thus, in the composite electrolytes, the SN molecules preferred to coordinate with the ANFs and the SiO_2—NH_2 nanoparticles, which can effectively inhibit the dipole-dipole interaction of SN and reduce the activity of α-H atoms to improve the electrochemical compatibility of SN with lithium metal.

Fourier transform infrared (FTIR) and ^{13}C nuclear magnetic resonance (NMR) spectroscopy measurements were carried out to deeply elaborate on the interaction between SN and other components of the composite electrolytes. Generally, the -C≡N stretching vibration band can be separated into two bands. The peak at 2252.3 cm^{-1} corresponded to free -C≡N, and another peak at 2259.3 cm^{-1} presented the coordinated nitrile groups with metal atoms and groups [23, 24]. In the SN-LiTFSI electrolyte, the -C≡N stretching vibration band only showed the free -C≡N peak. Two bands of -C≡N appeared in the CPE0 and CPE5 (Figure 2c,d). In the CPE0 system, the percentage of the coordinated nitrile groups was 37.4%, and the typical -NH characteristic peak of the ANF in the CPE0 was blue-shifted (Figure 2e; Figure S6), which indicated that there was a hydrogen-bond interaction between the -C≡N groups of SN and the -NH groups of the ANF [25]. In the CPE5 system, the -NH- characteristic peak of the ANF shifted an apparent shift from 1538.1 cm^{-1} to 1540.4 cm^{-1}, indicating that the hydrogen-bond interaction between the -C≡N groups of SN and the -NH groups of the ANF still existed. In addition, the -C═O peak of ANF showed a noticeable shift in ANF5, and the -NH_2 peaks of the SiO_2—NH_2 also shifted from 1404.7 cm^{-1} to 1406.3 cm^{-1}, which indicated that the -NH_2 groups of the SiO_2—NH_2 interacted with the -C═O groups of the ANF. In CPE5, the -C═O peak shifted to 1644.9 cm^{-1} and the —NH_2 peaks of the SiO_2—NH_2 at 1404.7 cm^{-1} disappeared, implying that the -NH_2 peaks of the SiO_2—NH_2 in the composite electrolyte tended to form a hydrogen-bond interaction with the -C≡N groups of SN rather than the -C═O groups of the ANF. Thereby, the percentage of the coordinated nitrile groups increased to 63.5%, which was higher than that of the CPE0 (Figure 2c,d). Moreover, the vibration peak of the -CH_2- groups of SN at 1424.7 cm^{-1} showed a nonobvious change, suggesting that the electron-rich -C═O groups primarily coordinated with Li^+ and facilitated Li^+ transport in composite electrolytes (Figure 2e).

These results demonstrated that the -NH groups of the ANF or -NH_2 groups of the SiO_2—NH_2 can directly coordinate with the -C≡N groups of SN to form multiple hydrogen-bonds and effectively reduce the activity of the α-H atom in SN, further hindering the side-reaction between SN and Li metal. The ^{13}C NMR peak of -C≡N groups in SN delivered a significant displacement from 116.13 ppm in the CPE0 to 116.24 ppm in the

16136829, 2026, 29, Downloaded from https://onlinelibrary.wiley.com/doi/10.1002/smll.73296 by North China Electric Power University Beijing, Wiley Online Library on [08/10/2026]. See the Terms and Conditions (https://onlinelibrary.wiley.com/terms-and-conditions) on Wiley Online Library for rules of use; OA articles are governed by the applicable Creative Commons License

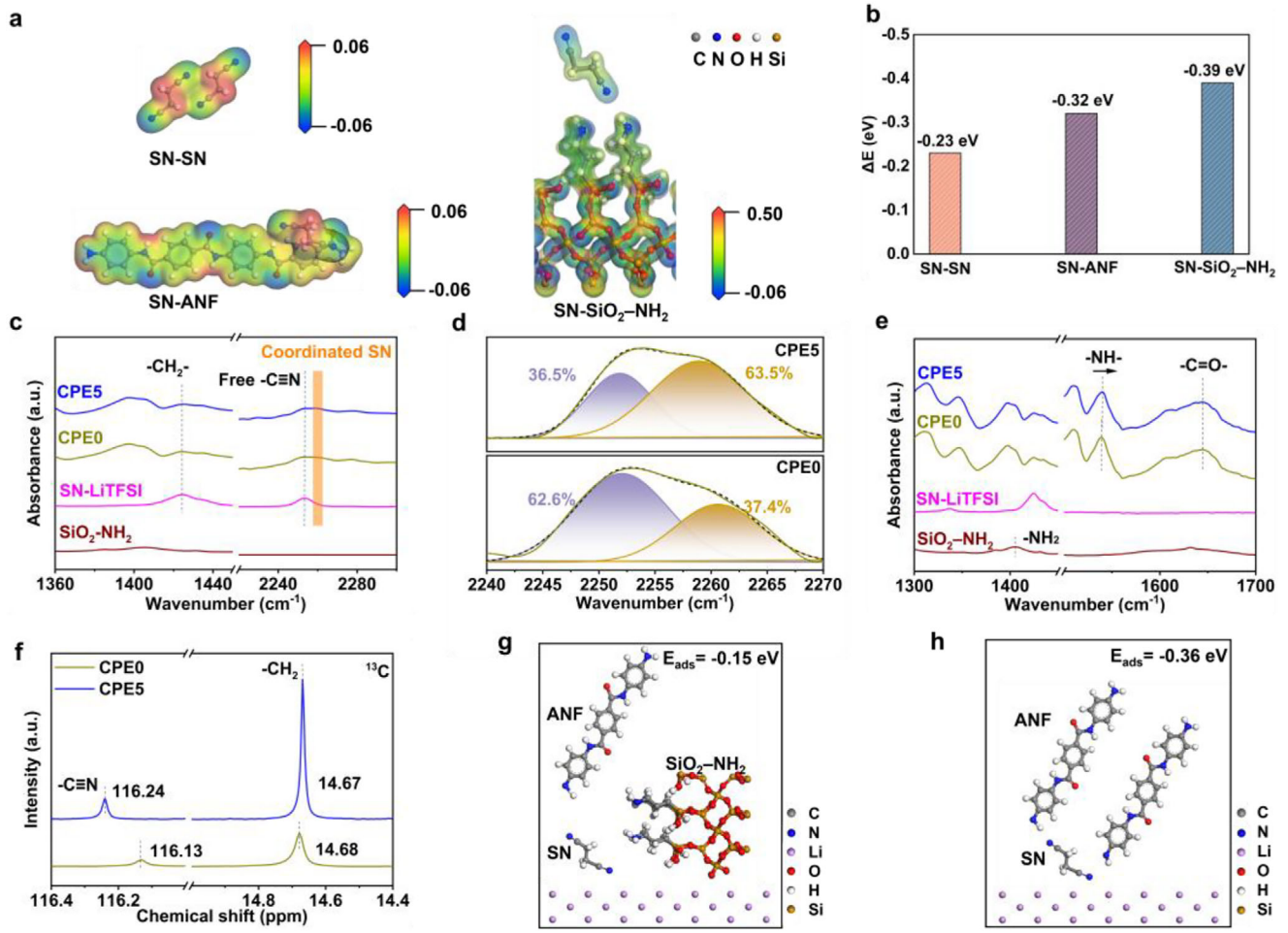


FIGURE 2 | The understanding of the roles of the hydrogen bonds. (a) The optimized geometric configurations and electrostatic potential of SN-SN, SN-ANF, and SN-SiO_2—NH_2. (b) The binding energy of SN-SN, SN-ANF, and SN-SiO_2—NH_2. (c–e) FTIR spectra of SiO_2—NH_2, SN-LiTFSI, CPE0, and CPE5. (f) ^{13}C NMR spectra of CPE0 and CPE5. (g, h) Adsorption of SN molecules on Li metal surfaces.

CPE5 (Figure 2f), but the peak of -CH_2 groups in SN showed no remarkable change, which was consistent with the FTIR results.

Furthermore, to investigate the chemical compatibility of SN with lithium metal in composite electrolyte-based LMBs, the adsorption energies of SN on the Li metal surface were also calculated. The adsorption energy (—0.15 eV) of SN with the Li metal in the CPE5 system is much higher than that in the CPE0 system (—0.36 eV), demonstrating that the hydrogen-bond interaction between the -C≡N groups of SN and the -NH_2 groups of the SiO_2—NH_2 can greatly reduce the adsorption of SN on Li metal and inhibit the decomposition of SN due to the catalysis of the Li metal (Figure 2g,h).

2.3 | Electrochemical, Mechanical, and Thermal Properties of the Electrolytes

Temperature-dependent ionic conductivity of the composite electrolytes was measured in a temperature range from −20 to 80°C. With the addition of the SiO_2—NH_2 nanofillers, the composite electrolytes showed an increasing ionic conductivity. However, due to the agglomeration of the nanoparticles in the CPE10, the CPE5 membranes exhibited the highest lithium ionic conductivity over a wide temperature range (Figure 3a; Table S2). Even at low temperatures, the CPE5 still delivered considerable ionic conductivity (e.g., 3.14×10^{-4} S cm^{-1} at 0°C, Figure 3b). Generally, composite electrolytes with lower crystallinity showed higher ionic conductivity. In X-ray diffraction (XRD) patterns, there were no obvious characteristic peaks of the SN (~19° and 29°) in composite electrolytes, indicating that the whole SN-based electrolyte matrix was mostly amorphous (Figure 3c). Besides, ANF with many polar groups (i.e., -C═O) also showed lower crystallinity after the addition of the nanoparticles and SN-LiTFSI matrix. This would be beneficial for the Li^+ transport in the composite electrolytes. Differential scanning calorimetry (DSC) measurements further revealed the roles of the SiO_2—NH_2 nanofillers in the composite electrolytes. The melting point (T_m) peak of the SN-LiTFSI matrix (39.2°C) obviously disappeared, and the transition temperature (T_{cp}) from normal crystal to plastic crystal phase (—37.4°C) decreased in the composite electrolytes (Figure S7). In addition, the T_{cp} of the CPE5 (—46.5°C) was lower than that of CPE0 (—40.9°C), again demonstrating that the crystallinity of the SN-LiTFSI was effectively reduced because of the existence of the SiO_2—NH_2 nanofillers (Figure 3d). The decrease in crystallinity indicated an accelerated SN molecule isomer transition rate from gauche to trans and an increased defect density, which could

16136829, 2026, 29, Downloaded from https://onlinelibrary.wiley.com/doi/10.1002/smll.73296 by North China Electric Power University Beijing, Wiley Online Library on [08/10/2026]. See the Terms and Conditions (https://onlinelibrary.wiley.com/terms-and-conditions) on Wiley Online Library for rules of use; OA articles are governed by the applicable Creative Commons License

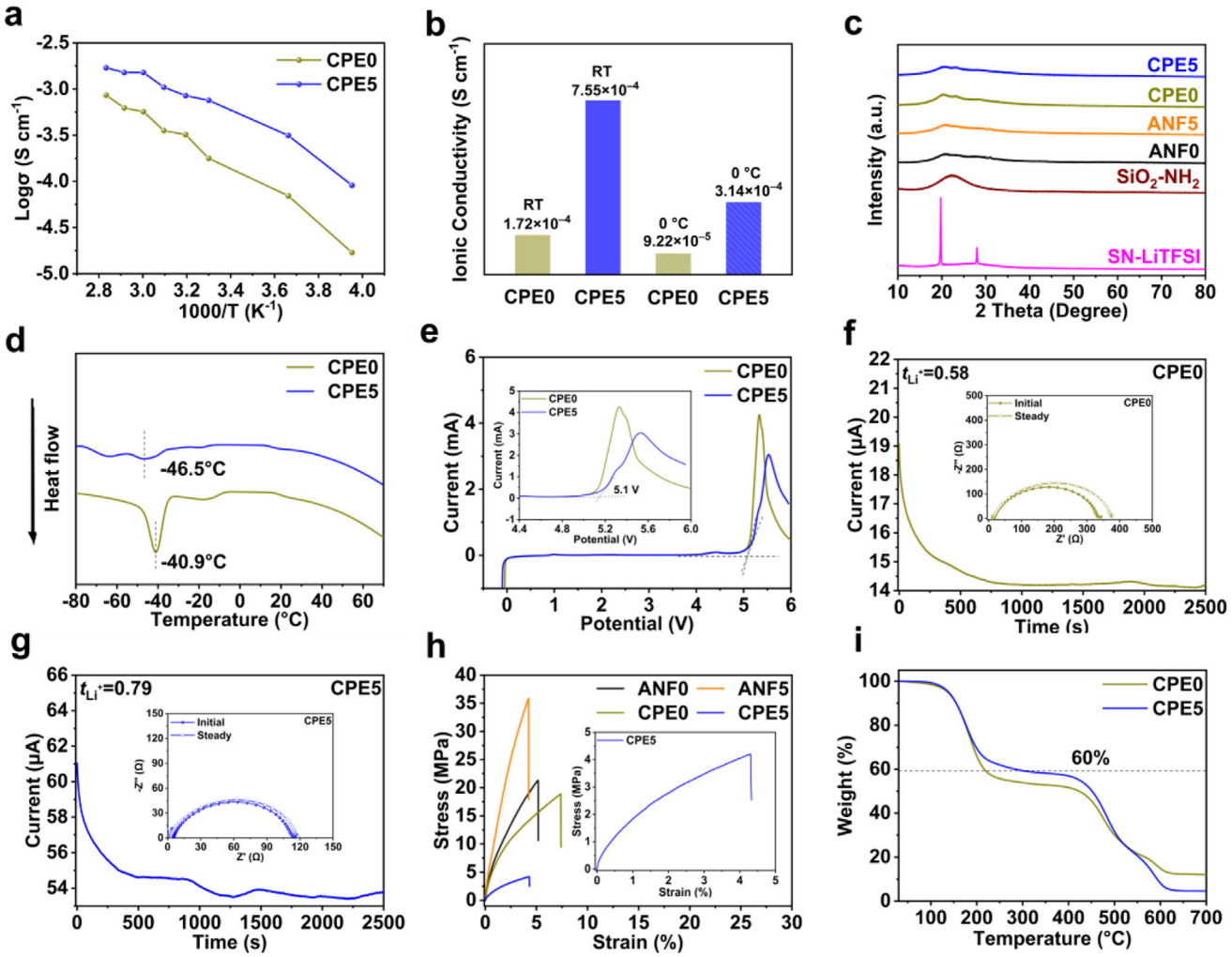


FIGURE 3 | The performance of the composite electrolytes. (a) Ionic conductivity of the electrolyte membranes. (b) Room temperature and 0°C ionic conductivity. (c) XRD patterns of the SiO_2—NH_2, SN-LiTFSI electrolyte, and composite electrolytes. (d) DSC curves of the composite electrolytes. (e) Liner sweep voltammetry (LSV) curves of the composite electrolytes. (f, g) The chronoamperometry (CA) curves at 30°C and 0.01 V (The inset was the Nyquist charts before and after the polarization). (h) Mechanical tensile stress/strain curves of the electrolyte membranes. (i) TGA curves of the composite electrolyte membranes.

facilitate Li^+ transport and enhance the ionic conductivity of electrolytes.

The electrochemical stability window is an indispensable parameter for high working potential LMBs. As shown in Figure 3e, compared with the CPE0, the CPE5 displayed a remarkably expanded oxidation potential of 5.1 V at 30°C. In addition to the high ionic conductivity, the CPE5 showed a much higher Li^+ transference number (t_{Li+}) than the CPE0 (0.79 vs 0.58, Figure 3f,g), which could decrease the overpotential and improve the rate capability of the cells. The increased t_{Li+} values also suggested that free $TFSI^-$ might be immobilized by the amino-functional SiO_2 particles with a large specific surface area. The Lewis acid center of the nanofillers can accelerate the LiTFSI dissociation and facilitate the Li^+ release, further enhancing the Li^+ conduction process [20].

The tensile strengths of the substrate films with and without the SiO_2—NH_2 nanofillers were measured to be 35.9 and 21.3 MPa, respectively (Figure 3h; Figure S8). The incorporation of the SiO_2—NH_2 nanofillers can effectively enhance the mechanical strength of the porous substrate films through the hydrogen-bond interaction between the -NH_2 groups of the SiO_2—NH_2 nanofillers and the amide groups of the ANFs. With the introduction of the SN-LiTFSI electrolyte, the tensile strength of the CPE5 membranes decreased to 4.2 MPa. It was shown that the -C≡N groups of SN were more likely to form hydrogen-bond interaction with the -NH_2 groups of the nanofillers and the -NH groups of the ANFs (Figure 2c–e). These hydrogen-bonds can destroy the coordination between the ANF chains and the SiO_2—NH_2 nanofillers, resulting in the reduction of the mechanical strength of the CPE5. However, the mechanical strength of the CPE5 membranes still affords the battery work requirement [26–31].

Furthermore, the composite electrolytes presented good thermal stability by thermogravimetric analysis (TGA) (Figure 3i). The decomposition of SN started at around 180°C in both CPE0 and CPE5. Apparently, the CPE5 showed superior thermostability compared with the CPE0 in the temperature range of 230–420°C, indicating that the hydrogen-bond interaction between -C≡N

16136829, 2026, 29, Downloaded from https://onlinelibrary.wiley.com/doi/10.1002/smll.73296 by North China Electric Power University Beijing, Wiley Online Library on [08/10/2026]. See the Terms and Conditions (https://onlinelibrary.wiley.com/terms-and-conditions) on Wiley Online Library for rules of use; OA articles are governed by the applicable Creative Commons License

of SN and -NH_2 of the nanofillers can weaken the decomposition of the electrolytes. The LiTFSI decomposition occurred at 420°C. While the temperature increased above 500°C, due to the degradation of the -CO—NH and aromatic-NH bonds with subsequent decarboxylation of carbonyl end groups, all the composite electrolytes showed a certain amount of weight loss [32, 33]. The CPE5 displayed a significant weight loss compared to the CPE0, indicating that the introduction of the SiO_2—NH_2 nanofillers weakened the hydrogen-bond interaction between the amide groups of the ANFs and resulted in the easy decomposition of the ANFs at above 500°C. Meanwhile, the thermal shrinkage behavior was also carried out to investigate the thermostability of the composite electrolytes (Figure S9). After storage at 160°C in air for 0.5 h, the commercial separator presented remarkable shrinkage. In contrast, the composite electrolyte membranes (especially the CPE5) still maintained the original shape even after 3 h, which can be attributed to the good thermal property of the ANFs and the hydrogen-bond interaction between the ANFs, the SiO_2—NH_2 nanofillers, and the SN-LiTFSI electrolyte.

2.4 | Interfacial Compatibility with Lithium Metal

As previously mentioned, SN undergoes severe side reactions with Li metal (the polymerization of nitrile groups). To evaluate the interface compatibility between the SN-based composite electrolytes and lithium metal, the composite electrolyte-based symmetric Li||Li cells were assembled and tested at 30°C. As shown in Figure 4a, the cell using the CPE0 exhibited a higher initial overpotential than that of the CPE5-based symmetric cells. With the increase in cycling time, the Li|CPE0|Li cell suffered a rapid voltage increase, indicating the growth of lithium dendrites and gradual accumulation of the SEI layer. However, under a current density of 0.1 mA cm^{-2}, the cell using the CPE5 was stable even over 2600 h with a low overpotential (<300 mV). As shown in the electrochemical impedance spectroscopy (EIS) spectra (Figure S10), the interfacial impedance of the Li|CPE0|Li cell increased to 1780 Ω after 300 cycles, indicating the numerous accumulations of side products on the lithium metal surface. On the contrary, the interfacial impedance of the symmetrical cell using the CPE5 only increased to 260 Ω, demonstrating the easy lithium ion migration at the electrode/electrolyte interphases in the CPE5-based cells. In addition, the critical current density (CCD) of the various electrolyte-based Li||Li cells was also tested (Figure 4b,c). The CPE5-based cell delivered a higher critical tolerance (1.1 mA cm^{-2}) than the CPE0-based cell (1.0 mA cm^{-2}).

To further evaluate the interface compatibility between the composite electrolytes and the lithium metal electrodes, the morphology changes of the composite electrolytes and the lithium electrodes after 700 h cycling at 0.1 mA cm^{-2} were detected by SEM. As shown in Figure 4d, the surfaces of the cycled CPE0 membranes had a lot of deposited microparticles and large protrusions. In stark contrast, the cycled CPE5 membranes were much smoother. Similarly, plenty of Li dendrites and cracks appeared on the lithium electrodes in the Li|CPE0|Li cell. However, the Li metal from the CPE5 symmetric cell remained flat without any obvious cracks (Figure 4e). Moreover, the SEI layers on the lithium electrodes after the cycling were characterized by X-ray photoelectron spectroscopy (XPS) to further reveal the reason for the excellent compatibility between the CPE5 and the lithium metal (Figure 4f). The SEI layers in the CPE0-based cells showed the presence of a Li—N—C peak, which was ascribed to the reduction of SN (the polymerization of nitrile groups) [4, 34, 35]. The interfaces between the CPE5 and the lithium metals formed a passive layer rich in Li_3N. Li_3N is a Li^+ conductor and can regulate the deposition of Li^+. This Li_3N-rich layer would promote uniform lithium deposition and enhance the interphase stability between electrolytes and lithium metal. However, the SEI layers in the CPE0-based cell contained less LiF, indicating that the slower Li^+ transport during the plating and stripping [3]. Combining the SEM and XPS results, it is easy to conclude that the CPE5 with abundant hydrogen bonds can form a stable SEI layer on the lithium electrodes during the cycling process, greatly inhibiting the growth of lithium dendrites.

2.5 | Lithium Metal Battery Performance

All-solid-state LMBs were assembled with $LiFePO_4$ (LFP) cathodes to evaluate the practical feasibility of the composite electrolytes. The cyclic voltammograms of the Li||LFP cells with different electrolytes at 0.1 mV s^{-1} are shown in Figure S11. The Li|CPE5|LFP cell showed higher peak currents than the CPE0-based cell, suggesting more rapid electrochemical reactions in the cell [12, 36]. The Li||LFP cells with the composite electrolytes exhibited an excellent rate performance at 30°C (Figure 5a). The discharge specific capacities of the Li|CPE5|LFP cell at 0.1 C, 0.2 C, 0.3 C, and 0.5 C were at 156.5 mAh g^{-1}, 152.0 mAh g^{-1}, 150.2 mAh g^{-1}, and 145.7 mAh g^{-1}, respectively. Notably, the discharge capacity of the Li|CPE5|LFP cell restored to 150.8 mAh g^{-1} when the current density returned to 0.2 C. The long-term cycling performance of the Li||LFP cells was shown in Figure 5b. The Li||LFP cell with the CPE5 displayed a stable cycling performance with a high-capacity retention of 80% after 700 cycles. The charge-discharge voltage curves of the Li|CPE5|Li cell were smooth, and the overpotential was almost unchanged (Figure 5c). In contrast, the Li|CPE0|LFP cell suffered a capacity decay after 300 cycles, and the overpotential significantly increased during the continuous cycling process (Figure 5b; Figure S12). In addition, the impedance of the Li|CPE0|LFP cell increased to 1877 Ω after 300 cycles, indicating the numerous accumulations of side products at the electrolyte/electrode interphases (Figure 5d; Figure S13). In comparison, the impedance of the Li||LFP cell using the CPE5 only increased to 820 Ω, demonstrating the easier lithium ion migration between the electrolytes and the electrodes.

The stable operation of the LMBs without obvious performance degradation over a wide temperature range is a key issue in current battery research and development. Considering the impressive ionic conductivity of the CEP5 at low temperatures (e.g., 9.06×10^{-5} S cm^{-1} at −20°C), the Li|CPE5|LFP cell was measured under extremely harsh working conditions to demonstrate the environmental adaptability of the composite electrolytes. As shown in Figure 5f, the discharge capacities of the Li|CPE5|LFP cell at 0.2 C were 157.9 mAh g^{-1}, 134.4 mAh g^{-1}, 108.9 mAh g^{-1}, and 78.2 mAh g^{-1} at 30°C, 0°C, −10°C and −20°C, respectively. Additionally, the discharge capacity recovered to 156.4 mAh g^{-1} when the temperature increased to 30°C again, demonstrating the superior lithium ions transport properties of the CPE5. However, the Li|CPE0|LFP cell displayed inferior discharge capacities at

16136829, 2026, 29, Downloaded from https://onlinelibrary.wiley.com/doi/10.1002/smll.73296 by North China Electric Power University Beijing, Wiley Online Library on [08/10/2026]. See the Terms and Conditions (https://onlinelibrary.wiley.com/terms-and-conditions) on Wiley Online Library for rules of use; OA articles are governed by the applicable Creative Commons License

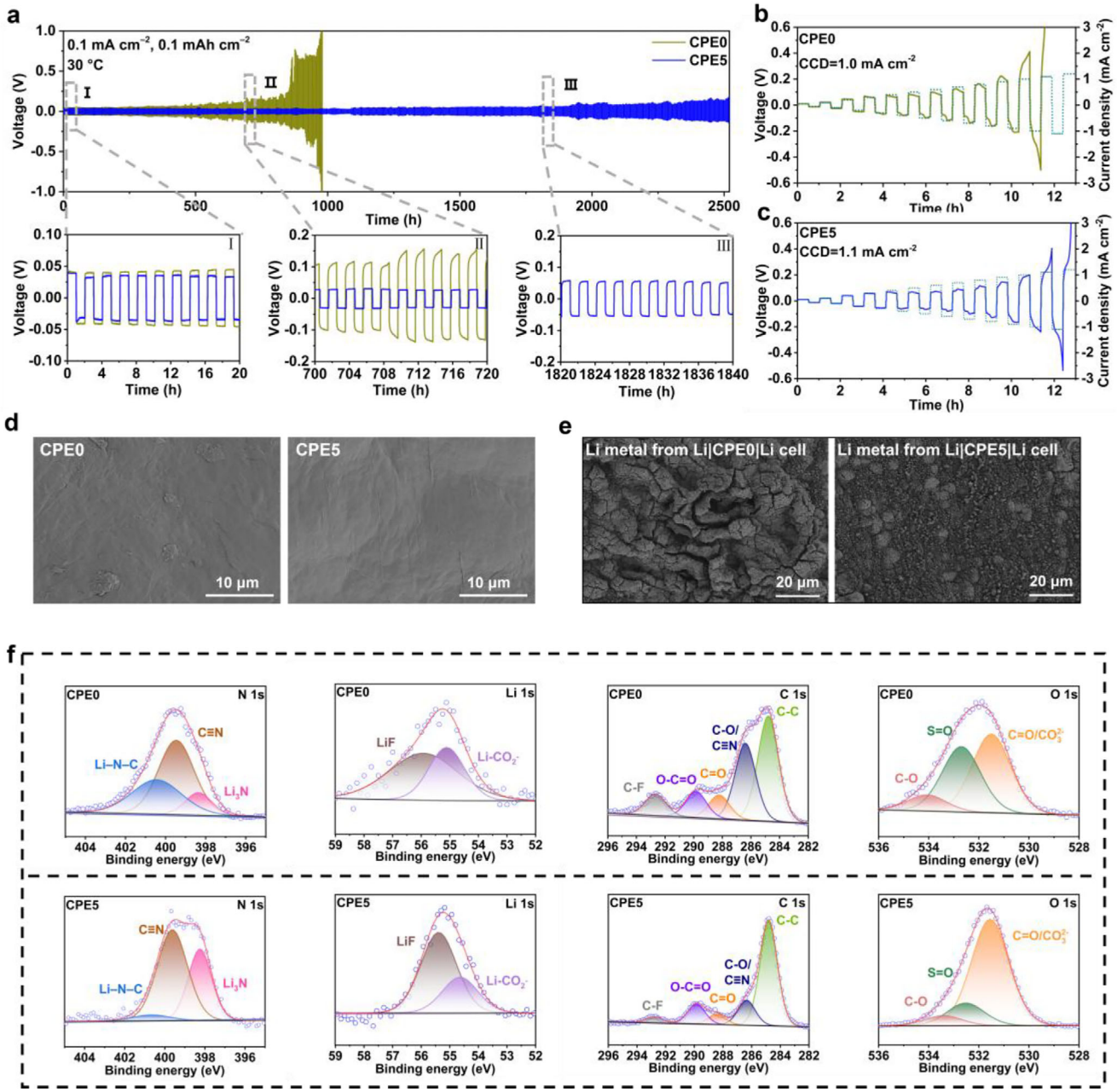


FIGURE 4 | The Li||Li symmetrical cells performance. (a) Long-term plating/stripping curves of the Li|CPE0|Li and Li|CPE5|Li cells at 0.1 mA cm^{-2}, and the segments of the iconic curves are marked as I, II, and III. (b, c) Critical current density of the Li||Li cells from 0.05 to 1.2 mA cm^{-2}. (d) Surface morphologies for the cycled composite electrolytes in Li||Li cells. (e) Surface morphologies for the cycled Li electrodes in Li||Li cells. (f) XPS spectra of the cycled Li electrodes from the symmetric batteries.

low temperatures (Figure 5e). When cycled at 0°C, after the activation at 0.1 C for 3 cycles, the CPE0-based cell showed an initial discharge capacity of 125.4 mAh g^{-1} and then experienced a quick decrease in capacity to 19.8 mAh g^{-1} within 10 cycles (Figure 5g). Nevertheless, the Li|CPE5|LFP cell displayed a steady cycling process for more than 700 cycles with a high-capacity retention of 96% (Figure 5f). The above results confirmed that the CPE5 was more compatible with lithium metal and suitable for large-scale application in low temperature conditions (Figure 5g).

The solid-state Li|| $LiNi_{0.6}Co_{0.2}Mn_{0.2}O_2$ (NCM622) cells were also tested at a wide cutoff voltage window of 2.8–4.25 V to further investigate their practical application. As illustrated in Figure 6a, the Li||NCM622 cell with the CPE0 exhibited poor rate performance with the discharge capacities of 166.0 mAh g^{-1}, 153.6 mAh g^{-1}, 146 mAh g^{-1}, 124.7 mAh g^{-1}, and 69.5 mAh g^{-1} at 0.1 C, 0.2 C, 0.3 C, 0.5 C, and 1.0 C, respectively. In stark contrast, the CPE5-based Li||NCM622 cell displayed higher discharge capacities of 129.1 and 84.0 mAh g^{-1} at 0.5 C and 1.0 C, respectively, and the discharge capacity recovered to 151.7 mAh g^{-1} when the current density returned to 0.2 C. Compared with the Li|CPE0|NCM622 cell, the charge and discharge voltages of the CPE5-based cell were relatively stable over cycling (Figure 6b,c), which was attributed to the

16136829, 2026, 29, Downloaded from https://onlinelibrary.wiley.com/doi/10.1002/smll.73296 by North China Electric Power University Beijing, Wiley Online Library on [08/10/2026]. See the Terms and Conditions (https://onlinelibrary.wiley.com/terms-and-conditions) on Wiley Online Library for rules of use; OA articles are governed by the applicable Creative Commons License

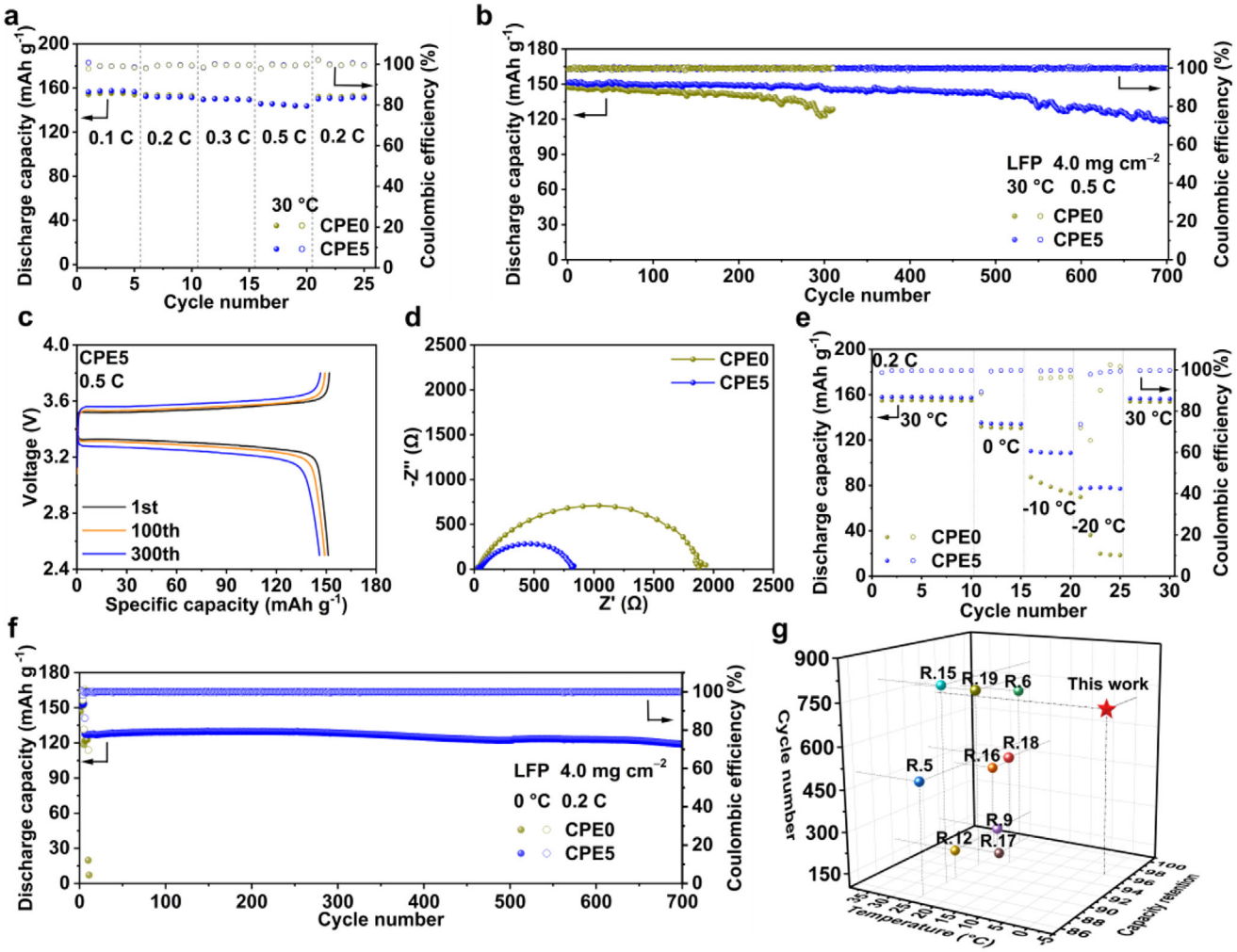


FIGURE 5 | Electrochemical performance of Li||LFP cells. (a) Rate performance and (b) cycling performance of the solid-state Li||LFP cells. (c) Typical charge–discharge voltage profiles of the solid-state Li||LFP cells. (d) EIS plots of the Li||LFP cells after 300 cycles at 0.5 C and 30°C. (e) Rate performance of the solid-state Li||LFP cells at 0.2 C and low temperatures. (f) Cycling performance of the solid-state Li||LFP cells at 0.2 C and 0°C. (g) The comparison of the capacity retention and the cycle number of the solid-state batteries (see details in Table S3).

highly conducive and kinetically favorable electrolyte/electrode interphases.

Furthermore, the long-term cycling performance of the solid-state Li||NCM622 cells with a high active material loading of 10 mg cm^{-2} was also investigated. The Li|CPE0|NCM622 cell showed a rapid capacity decrease at 0.3 C due to the serious side reaction between the electrolytes and the electrodes. However, the Li|CPE5|NCM622 cell delivered a higher capacity of 115.3 mAh g^{-1} and capacity retention of 75% after 150 cycles, indicating the exceptional performance of the CPE5 at a high-voltage battery system (Figure 6d). In addition, after 100 cycles, the impedance of the Li|CPE0|NCM622 cell increased from 140.8 to 478.8 Ω, whereas the Li|CPE5|NCM622 cell only increased to 249.9 Ω (Figure 6e), indicating the stable electrolyte-electrode interphase in the CPE5-based LMBs. The cell with the CPE5 also showed more stable voltages and higher charge/discharge capacity than the Li|CPE0|NCM622 cell (Figure 6f,g). A comprehensive comparison of the CPE0 and CPE5 was shown in Figure 6h, and the CPE5 delivered excellent properties (Table S3). We also found that the CPE5-based cells outperformed other solid-state batteries in recent reports, as far as we know (Table S4). These results demonstrated that the SN-based composite electrolyte containing ANFs and SiO_2–NH_2 nanoparticles showed great potential in solid-state LMBs.

3 | Conclusion

In summary, a novel strategy is developed to improve the electrochemical compatibility of SN with lithium metal by multiple hydrogen-bond interactions between the -C≡N groups of SN and the -NH_2 groups of the SiO_2—NH_2 and the -NH groups of the ANFs. In addition, this strategy promotes the formation of a uniform LiF-rich SEI layer, effectively enhancing the electrochemical performance of the LMBs. The composite electrolyte-based Li||Li cell stably cycles over 2600 h at room temperature, and the Li||LFP cell with the designed composite electrolyte also delivers a long cycle life over 700 cycles with a capacity retention of 96% at 0°C. Furthermore, the solid-state Li||NCM622 cell with a high active mass loading of 10 mg cm^{-2} displays excellent cycle performance. This work highlights the multiple hydrogen-bond

16136829, 2026, 29, Downloaded from https://onlinelibrary.wiley.com/doi/10.1002/smll.73296 by North China Electric Power University Beijing, Wiley Online Library on [08/10/2026]. See the Terms and Conditions (https://onlinelibrary.wiley.com/terms-and-conditions) on Wiley Online Library for rules of use; OA articles are governed by the applicable Creative Commons License

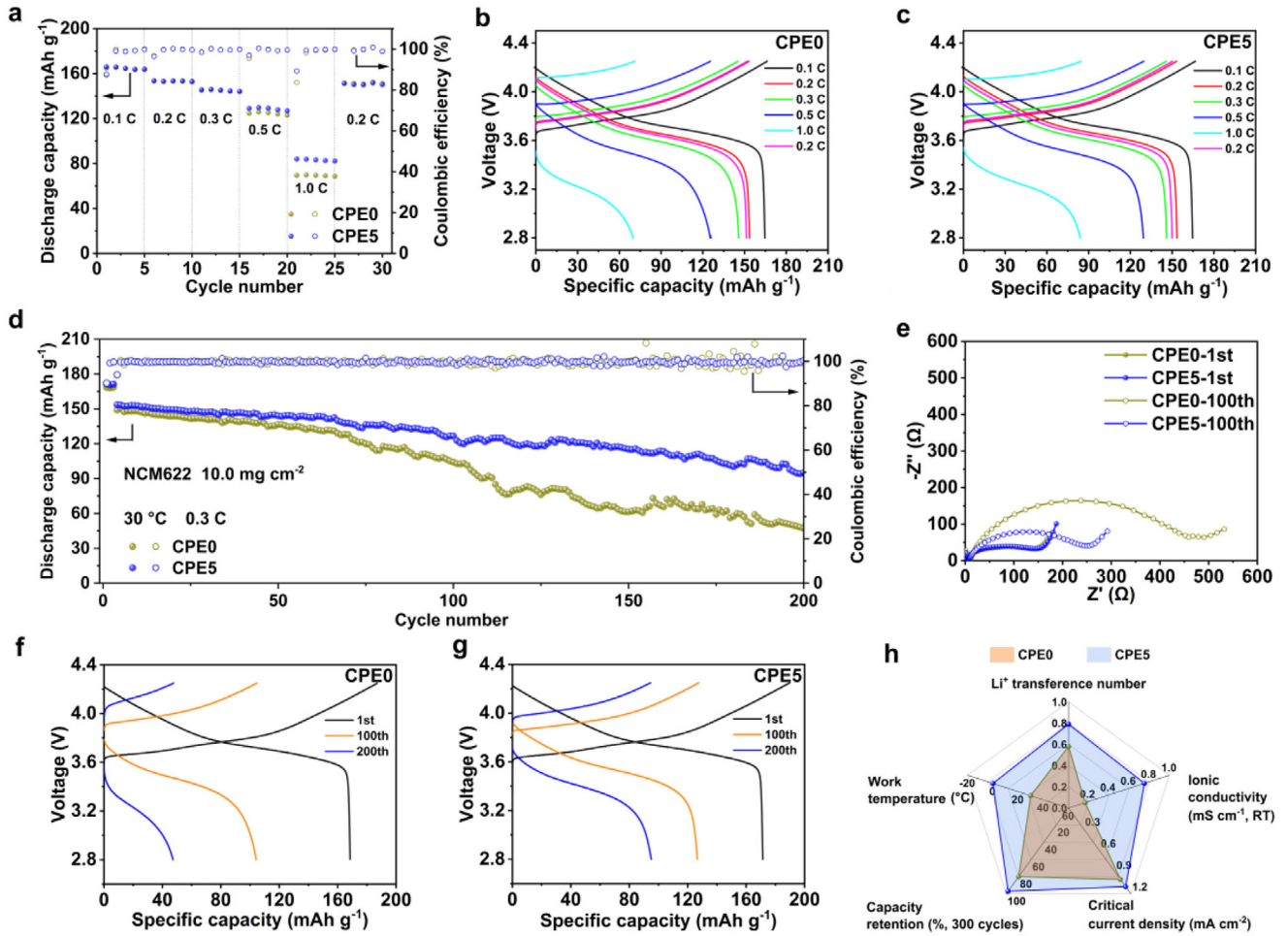


FIGURE 6 | Electrochemical performances of Li||NCM622 cells. (a) Rate performance of the solid-state Li||NCM622 cells. (b, c) Typical charge–discharge voltage profiles of the solid-state Li||NCM622 cells. (d) Cycling performance of the solid-state Li||LFP cells. (e) EIS plots of the Li||NCM622 cells. (f, g) Corresponding charge-discharge voltage profiles of the two cells. (h) Radar map of the physicochemical properties of two electrolytes (see details in Table S4).

interaction effect and offers a new design principle for SN-based solid-state LMBs.

Acknowledgements

This work is supported partially by project of National Natural Science Foundation of China (52272200, 52302250), Hebei Natural Science Foundation (E2022502022), the Project of China Three Gorges Corporation named Key Technologies of Intelligent Joint Regulation and Operation with grid connected friendly in power station group of wind, solar photovoltaic and energy storage (WWKY-2021-0173), Huaneng Group Headquarters Science and Technology Project (HNKJ20-H88), and the NCEPU "Double First-Class" Program.

Conflicts of Interest

The authors declare no conflict of interest.

Data Availability Statement

The data that support the findings of this study are available from the corresponding author upon reasonable request.

References

1. C. Zhang, S. Gamble, D. Ainsworth, A. M. Z. Slawin, Y. G. Andreev, and P. G. Bruce, "Alkali Metal Crystalline Polymer Electrolytes," *Nature Materials* 8 (2009): 580–584, https://doi.org/10.1038/nmat2474.

2. Y. Wang, C. J. Zanelotti, X. E. Wang, et al., "Solid-State Rigid-Rod Polymer Composite Electrolytes with Nanocrystalline Lithium Ion Pathways," *Nature Materials* 20 (2021): 1255–1263, https://doi.org/10.1038/s41563-021-00995-4.

3. X. Yang, K. R. Adair, X. Gao, and X. Sun, "Recent Advances and Perspectives on Thin Electrolytes for High-Energy-Density Solid-State Lithium Batteries," *Energy & Environmental Science* 14 (2021): 643–671, https://doi.org/10.1039/D0EE02714F.

4. M. J. Lee, J. Han, K. Lee, et al., "Elastomeric Electrolytes for High-Energy Solid-State Lithium Batteries," *Nature* 601 (2022): 217–222, https://doi.org/10.1038/s41586-021-04209-4.

5. W. Chen, H. Duan, J. Shi, et al., "Bridging Interparticle Li + Conduction in a Soft Ceramic Oxide Electrolyte," *Journal of the American Chemical Society* 143 (2021): 5717–5726, https://doi.org/10.1021/jacs.0c12965.

6. L. Tang, B. Chen, Z. Zhang, et al., "Polyfluorinated Crosslinker-Based Solid Polymer Electrolytes for Long-Cycling 4.5 V Lithium Metal Batteries," *Nature Communications* 14 (2023): 2301, https://doi.org/10.1038/s41467-023-37997-6.

16136829, 2026, 29, Downloaded from https://onlinelibrary.wiley.com/doi/10.1002/smll.73296 by North China Electric Power University Beijing, Wiley Online Library on [08/10/2026]. See the Terms and Conditions (https://onlinelibrary.wiley.com/terms-and-conditions) on Wiley Online Library for rules of use; OA articles are governed by the applicable Creative Commons License

7. J. Xu, J. Zhang, T. P. Pollard, et al., "Electrolyte Design for Li-Ion Batteries Under Extreme Operating Conditions," *Nature* 614 (2023): 694–700, https://doi.org/10.1038/s41586-022-05627-8.

8. C. Su, Y. Qu, N. Hu, et al., "Rapid Na^+ Transport Pathway and Stable Interface Design Enabling Ultralong Life Solid-State Sodium Metal Batteries," *Angewandte Chemie, International Edition* 64 (2025): 202418959.

9. J. Zhang, H. Wu, X. Du, et al., "Smart Deep Eutectic Electrolyte Enabling Thermally Induced Shutdown Toward High-Safety Lithium Metal Batteries," *Advanced Energy Materials* 13 (2023): 2202529, https://doi.org/10.1002/aenm.202202529.

10. P.-J. Alarco, Y. Abu-Lebdeh, A. Abouimrane, and M. Armand, "The Plastic-Crystalline Phase of Succinonitrile as a Universal Matrix for Solid-State Ionic Conductors," *Nature Materials* 3 (2004): 476–481, https://doi.org/10.1038/nmat1158.

11. K. H. Choi, S. J. Cho, S. H. Kim, Y. H. Kwon, J. Y. Kim, and S. Y. Lee, "Thin, Deformable, and Safety-Reinforced Plastic Crystal Polymer Electrolytes for High-Performance Flexible Lithium-Ion Batteries," *Advanced Functional Materials* 24 (2014): 44–52, https://doi.org/10.1002/adfm.201301345.

12. J. Chen, Z. Yang, X. Xu, et al., "Nonflammable Succinonitrile-Based Deep Eutectic Electrolyte for Intrinsically Safe High-Voltage Sodium-Ion Batteries," *Advanced Materials* 36 (2024): 2400169, https://doi.org/10.1002/adma.202400169.

13. C. Fu, Y. Ma, S. Lou, et al., "A Dual-Salt Coupled Fluoroethylene Carbonate Succinonitrile-Based Electrolyte Enables Li-Metal Batteries," *Journal of Materials Chemistry A* 8 (2020): 2066–2073, https://doi.org/10.1039/C9TA11341J.

14. J. Zheng, M. H. Engelhard, D. Mei, et al., "Electrolyte Additive Enabled Fast Charging and Stable Cycling Lithium Metal Batteries," *Nature Energy* 2 (2017): 17012, https://doi.org/10.1038/nenergy.2017.12.

15. H. Wu, B. Tang, X. F. Du, et al., "LiDFOB Initiated In Situ Polymerization of Novel Eutectic Solution Enables Room-Temperature Solid Lithium Metal Batteries," *Advanced Science* 7 (2020): 2003370, https://doi.org/10.1002/advs.202003370.

16. D. Bao, Y. Tao, Y. Zhong, et al., "High-Performance Dual-Salt Plastic Crystal Electrolyte Enabled by Succinonitrile-Regulated Porous Polymer Host," *Advanced Functional Materials* 33 (2023): 2213211, https://doi.org/10.1002/adfm.202213211.

17. C. Kang, J. Zhu, Y. Wang, et al., "Concentration Induced Modulation of Solvation Structure for Efficient Lithium Metal Battery by Regulating Energy level of LUMO Orbital," *Energy Storage Materials* 61 (2023): 102898, https://doi.org/10.1016/j.ensm.2023.102898.

18. K. Liu, F. Ding, J. Q. Liu, et al., "A Cross-Linking Succinonitrile-Based Composite Polymer Electrolyte With Uniformly Dispersed Vinyl-Functionalized SiO_2 Particles for Li-Ion Batteries," *ACS Applied Materials & Interfaces* 8 (2016): 23668–23675, https://doi.org/10.1021/acsami.6b05882.

19. A. Wang, S. Geng, Z. Zhao, Z. Hu, and J. Luo, "In Situ Cross-Linked Plastic Crystal Electrolytes for Wide-Temperature and High-Energy-Density Lithium Metal Batteries," *Advanced Functional Materials* 32 (2022): 2201861, https://doi.org/10.1002/adfm.202201861.

20. K. Liu, H. Cheng, Z. Wang, et al., "A 3 μm-Ultrathin Hybrid Electrolyte Membrane with Integrative Architecture for All-Solid-State Lithium Metal Batteries," *Advanced Energy Materials* 14 (2024): 2303940, https://doi.org/10.1002/aenm.202303940.

21. B. Yang, L. Wang, M. Y. Zhang, J. J. Luo, Z. Q. Lu, and X. Y. Ding, "Fabrication, Applications, and Prospects of Aramid Nanofiber," *Advanced Functional Materials* 30 (2020): 2000186, https://doi.org/10.1002/adfm.202000186.

22. C. J. Xie, Z. X. Guo, T. Qiu, and X. L. Tuo, "Construction of Aramid Engineering Materials via Polymerization-Induced para -Aramid Nanofiber Hydrogel," *Advanced Materials* 33 (2021): 2101280, https://doi.org/10.1002/adma.202101280.

23. M. J. Katz, P. M. Aguiar, R. J. Batchelor, et al., "Structure and Multinuclear Solid-State NMR of a Highly Birefringent Lead–Gold Cyanide Coordination Polymer," *Journal of the American Chemical Society* 128 (2006): 3669–3676, https://doi.org/10.1021/ja0566634.

24. Y.-N. Yang, F.-L. Jiang, Y.-Q. Li, Z.-X. Wang, and T. Zhang, "Inside Cover: A Surface Coordination Interphase Stabilizes a Solid-State Battery (Angew. Chem. Int. Ed. 45/2021)," *Angewandte Chemie International Edition* 60 (2021): 23922, https://doi.org/10.1002/anie.202111739.

25. D. Zhang, X. Meng, W. Zhang, et al., "A Thin and Ultrahigh-Ionic-Conductivity Composite Electrolyte with 3D Aramid Nanofiber Networks Toward Ambient-Temperature Lithium Metal Batteries," *Advanced Energy Materials* 15 (2025): 2403565, https://doi.org/10.1002/aenm.202403565.

26. L. Gao, S. B. Luo, J. X. Li, B. W. Cheng, W. M. Kang, and N. P. Deng, "Core-Shell Structure Nanofibers-Ceramic Nanowires Based Composite Electrolytes with High Li Transference Number for High-Performance All-Solid-State Lithium Metal Batteries," *Energy Storage Materials* 43 (2021): 266–274, https://doi.org/10.1016/j.ensm.2021.09.013.

27. Z. Wang, L. Shen, S. Deng, P. Cui, and X. Yao, "10 μm-Thick High-Strength Solid Polymer Electrolytes with Excellent Interface Compatibility for Flexible All-Solid-State Lithium-Metal Batteries," *Advanced Materials* 33 (2021): 2100353, https://doi.org/10.1002/adma.202100353.

28. F. He, W. Tang, X. Zhang, L. Deng, and J. Luo, "High Energy Density Solid State Lithium Metal Batteries Enabled by Sub-5 μm Solid Polymer Electrolytes," *Advanced Materials* 33 (2021): 2105329, https://doi.org/10.1002/adma.202105329.

29. S. Xia, B. Yang, H. Zhang, J. Yang, W. Liu, and S. Zheng, "Ultrathin Layered Double Hydroxide Nanosheets Enabling Composite Polymer Electrolyte for All-Solid-State Lithium Batteries at Room Temperature," *Advanced Functional Materials* 31 (2021): 2101168, https://doi.org/10.1002/adfm.202101168.

30. W. Liu, G. Li, W. Yu, et al., "Asymmetric Organic-Inorganic Bi-Functional Composite Solid-State Electrolyte for Long Stable Cycling of High-Voltage Lithium Battery," *Energy Storage Materials* 63 (2023): 103005, https://doi.org/10.1016/j.ensm.2023.103005.

31. Y. Liu, F. Fu, H. Teng, et al., "Dual-Phase Elastomeric Electrolyte With a Latitude-Longitude Interwoven Structure for High-Energy Solid-State Lithium Metal Batteries," *Advanced Energy Materials* 14 (2024): 2402040, https://doi.org/10.1002/aenm.202402040.

32. F. Wang, Y. Wu, Y. Huang, and L. Liu, "Strong, Transparent and Flexible Aramid Nanofiber/POSS Hybrid Organic/Inorganic Nanocomposite Membranes," *Composites Science and Technology* 156 (2018): 269–275, https://doi.org/10.1016/j.compscitech.2018.01.016.

33. A. M. Hindeleh and S. M. Abdo, "Effects of Annealing on the Crystallinity and Microparacrystallite Size of Kevlar 49 Fibres," *Polymer* 30 (1989): 218–224, https://doi.org/10.1016/0032-3861(89)90108-0.

34. C. Kang, J. Zhu, F. Kong, et al., "Low-Solvent-Coordination Solvation Structure for Lithium-Metal Batteries via Electric Dipole-Dipole Interaction," *Angewandte Chemie International Edition* 63 (2024): 202412703, https://doi.org/10.1002/anie.202412703.

35. H. Liu, Y. Liao, C. Leung, et al., "Ring-Opening Polymerization Reconfigures Polyacrylonitrile Network for Ultra Stable Solid-State Lithium Metal Batteries," *Advanced Energy Materials* 15 (2025): 2402795, https://doi.org/10.1002/aenm.202402795.

36. X. Zhou, Y. Huang, B. Wen, et al., "Regulation of Anion–Na^+ Coordination Chemistry in Electrolyte Solvates for Low-Temperature Sodium-Ion Batteries," *Proceedings of the National Academy of Sciences* 121 (2024): 2316914121, https://doi.org/10.1073/pnas.2316914121.

Supporting Information

Additional supporting information can be found online in the Supporting Information section.

Supporting file: smll73296-sup-0001-SuppMat.docx

16136829, 2026, 29, Downloaded from https://onlinelibrary.wiley.com/doi/10.1002/smll.73296 by North China Electric Power University Beijing, Wiley Online Library on [08/10/2026]. See the Terms and Conditions (https://onlinelibrary.wiley.com/terms-and-conditions) on Wiley Online Library for rules of use; OA articles are governed by the applicable Creative Commons License